Predicting fluorescence quantum yield for anisole at elevated temperatures and pressures

Q. Wang[1] · K. H. Tran[2] · C. Morin[3] · J. Bonnety[4] · G. Legros[4] · P. Guibert[4]

Abstract Aromatic molecules are promising candidates for using as a fluorescent tracer for gas-phase scalar parameter diagnostics in a drastic environment like engines. Along with anisole turning out an excellent temperature tracer by Planar Laser-Induced Fluorescence (PLIF) diagnostics in Rapid Compression Machine (RCM), its fluorescence signal evolution versus pressure and temperature variation in a high-pressure and high-temperature cell have been reported in our recent paper on Applied Phys. B by Tran et al. Parallel to this experimental study, a photophysical model to determine anisole Fluorescence Quantum Yield (FQY) is delivered in this paper. The key to development of the model is the identification of pressure, temperature, and ambient gases, where the FQY is dominated by certain processes of the model (quenching effect, vibrational relaxation, etc.). In addition to optimization of the vibrational relaxation energy cascade coefficient and the collision probability with oxygen, the non-radiative pathways are mainly discussed. The common non-radiative rate (intersystem crossing and internal conversion) is simulated in parametric form as a function of excess vibrational energy, derived from the data acquired at different pressures and temperatures from the literature. A new non-radiative rate, namely, the equivalent Intramolecular Vibrational Redistribution or Randomization (IVR) rate, is proposed to characterize anisole deactivated processes. The new model exhibits satisfactory results which are validated against experimental measurements of fluorescence signal induced at a wavelength of 266 nm in a cell with different bath gases (N_2, CO_2, Ar and O_2), a pressure range from 0.2 to 4 MPa, and a temperature range from 473 to 873 K.

1 Introduction

New concepts in Internal Combustion Engines (ICE) like gasoline direct injection, high boost pressures, and downsizing require detailed knowledge about the in-cylinder mixing processes and the local temperature to avoid fuel-rich pockets (leading to an increase of pollutant emission) or temperature variations that lead to uncontrolled knocking. The exact control of the mixture formation prior to ignition is one key step for this optimization. Optical diagnostic techniques like PLIF play an important role in monitoring these processes, because they are non-intrusive and exhibit high spatial and temporal resolutions. PLIF technique is used for the measurement of key parameters, such as the fuel concentration field [1], the temperature field [2] or fuel/air ratio [3], etc. that govern subsequent combustion efficiency and pollutant formation in new ICE. In general, the fluorescence signal simultaneously depends on temperature, pressure, and bath-gas composition. Therefore, it is of great importance to explore these dependences in test cells under well-defined thermodynamic conditions to provide the data required for quantitative diagnostics in practical applications.

✉ Q. Wang
  wangqianlong@sjtu.edu.cn

1 School of Mechanical Engineering, Shanghai Jiao Tong University, Shanghai, China

2 Laboratoire Energétique, Mécanique et Electromagnétisme, Université Paris Ouest, 50 rue de Sèvres, 92410 Ville d'Avray, Paris, France

3 LAMIH UMR CNRS 8201, UVHC, Le Mont Houy, 59313 Valenciennes cedex 9, France

4 UPMC Univ. Paris 06, UMR 7190, Inst. Jean Le Rond d'Alembert, Sorbonne University, 75005 Paris, France

For quantitative measurements, fluorescent tracers may be added to a non-fluorescing surrogate fuel. Ketones and aromatics are two commonly used groups of compounds [4]. For example, since the evaporation characteristics and transport properties of mono aromatic molecule (toluene, p-xylene, anisole, etc.) and polycyclic aromatic hydrocarbon (PAH) molecules (naphthalene, fluoranthene, etc.) are comparable to those of gasoline [5] and diesel [6] fuel, respectively, they can serve as tracers for those fuels. Indeed, there is a need for fair predictions of fluorescence signals from aromatics, such as benzene, naphthalene, or with a methyl/methoxy group, toluene/anisole, which are incorporated into surrogate gasoline or diesel fuel. Therefore, the developments of the FQY models pave the way for fluorescence quantitative simulation and scalar field visualization in future CFD. These aromatics are not only relevant tracers, due to their absorption features that can be measured with usual lasers and the relatively high fluorescence signal levels that they deliver, but they also play key roles in soot precursors formation processes. Recently, Menon [7] studied the small aromatic and large aromatic fluorescence images by PLIF when m-xylene was added to the ethylene diffusion flames and found m-xylene addition mainly contributed to the concentration of small PAH in the flame, not to larger aromatic compounds. Therefore, the adequate interpretation of fluorescence signal delivered by aromatic molecules eventually leads to more insights into the fundamental understanding of soot formation processes. Anisole (methoxybenzene, $C_6H_5OCH_3$) due to promising photophysical properties are successfully applied as a fluorescent tracer for temperature by LIF imaging [8–10], on which are deserved to shed more lights.

However, the interpretation of fluorescence signals at simultaneous high-temperature and high-pressure conditions is not straight forward, which leads to developing FQY models. Due to photophysical properties of different molecules, different models were developed [9, 11–15]. Thurber originally developed one photophysical model for acetone [14]. Later, Koch [13] further applied this model to 3-pentanone; meanwhile, a semi-empirical toluene model was also developed, which was a compromise between a complete representation of the physical processes involved in toluene fluorescence and a simple numerical fitting to the experimental data. Independently, since the higher sensitivity of aromatic to oxygen, the oxygen quenching processes were further interpreted by Rossow [15], who proposed the oxygen-induced vibrational relaxation rate within calculation probability of population transfer from higher levels in the semi-empirical toluene and naphthalene model. This oxygen-induced vibrational relaxation rate was assumed from the inefficient aromatic oxygen collisions. Recently, Cheung et al.

[12] introduced an additional new quenching rate, corresponding to quenching rate for collision with an inert gas like N_2. It is noted that one phenomenological anisole model was also reported by Faust et al. [9], which allowed the prediction of fluorescence lifetimes and relative FQY within a limited range of conditions relevant for typical tracer LIF applications. However, a photophysical model for anisole is still desirable for a better prediction of fluorescence intensities and lifetimes for temperature and pressure ranges as they anticipated.

Consequently, the prediction of fluorescence intensities or quantum yields for given environmental conditions can be carried out in three different ways. First, phenomenological or empirical models functional fits to experimental data by delivered the necessary information [9]. However, this procedure is strictly limited to the range of conditions, where the fit functions are applied. The generally rather simple fit functions allow an analysis of experimental data with low computational effort. The second way is the photophysical models [14], and they consider in detail the energy transfer processes taking place in each vibronic level in the excited state. If accurate enough, these models help to understand photophysical processes and deliver as by-product the same quantum yield information as the empirical models. As the advantage, their applicability may not be limited to conditions, where the model was validated but can be extended to experimentally unexplored temperature and pressure conditions. The information gathered about the photophysics of aromatic species allows us to extract data such as decay rates and fluorescence yields, which are required for the simulation of the cascading energy relaxation until the level of thermalisation is reached. The last one is a semi-empirical model that combines a development of the physical processes involved in fluorescence and some simple numerical fittings to the experimental data [12, 13, 15].

Within the framework of the previous studies, the original contribution of this present paper is to provide a semi-empirical FQY model for anisole, which is over a wide range of temperatures, pressures, and gas compositions within thermodynamic conditions close to those encountered into engines. Inspired by previous models developed for ketones, a basic photophysical model is introduced first. Optimizations of the common non-radiative rate, the collision probability with oxygen, and the vibrational relaxation for anisole consolidate this proposed model. A further milestone opening towards electronic deactivation through the Intramolecular Vibrational Redistribution is especially highlighted. Finally, this model is validated against experimental results of fluorescence signals obtained in a high-pressure and high-temperature cell.

2 Theoretical background and model description

The fluorescence quantum yield (Φ) is the ratio of photons absorbed to photons emitted through fluorescence. In other words, the overall quantum yield gives the probability of the excited state being deactivated by fluorescence rather than by other non-radiative mechanisms, and can be described by the following rate equation:

$$\Phi = \frac{k_{fl}}{k_{fl} + k_{vib} + k_{O_2} + k_{nr}}. \tag{1}$$

k_{fl} represents the fluorescence rate from the singlet state S_1, k_{nr} is the intramolecular non-radiative decay rate as the sum of decay rates intersystem crossing (ISC) and internal conversion (IC). While k_{vib} is vibrational relaxation rate corresponding to intermolecular collisional deactivation and k_{O2} is highlighted as the collisional oxygen quenching rate proportional to the oxygen number density.

When excited vibrational energy levels in the S_1 state are populated by absorption, a return to the vibrational level of thermal equilibrium in the electronic ground state S_0 is caused by different depopulation mechanisms. For either temperature or pressure changes, the FQY of ketone [11–15] or aromatic molecules [15–17] has been investigated for different excitation wavelengths. In general, a reduction in FQY with increasing temperature is found for the acetone and aromatic molecules. This phenomenon is explained by the enhanced common non-radiative rate on the higher vibrational energy level at the excited state, where the higher temperature reaches. The FQYs of lower vibrational levels are larger compared to those of higher vibrational levels. Provided that fluorescence signal intensity is enough high at a higher temperature, this larger drop dependence with temperature delivers a higher temperature detecting sensitivity by the PLIF technique.

On the other hand, with increasing pressure, the collision rate increases, and the initially populated highly excited vibrational levels (where there are high k_{nr} rates) are more quickly relaxed to low vibrational levels (where the k_{nr} rates are reduced). Thus, the observed pressure-related FQY increase for acetone and 3-pentanone arises from collisional effects. Conversely, with respect to some aromatics, e.g., toluene and anthracene, the opposite experimental results with lower FQY by increasing pressure were found [13, 18]. This is explained by the pressure destabilization effect that the bath-gas collisions lead to a "destabilization" in the sense that population is transferred into higher lying vibrational levels of S_1 and consequently results in a reduction of the probability of fluorescence emission. Benzler et al. [19] recently studied several one-and two-ring aromatics effective fluorescence lifetime at low pressure within temperature range of 296–475 K and indicated that the non-uniform pressure effect could be attributed to magnitudes comparison between the average energy of the initial distribution (E_1) and the thermal energy level $E_{thermal}^1$ at excited state S_1. The pressure destabilization effect is the laser-induced cooling, in the case of $E_{thermal}^1 > E_1$.

2.1 Step-ladder models

The step-ladder (photophysical) model for the calculation of the FQY was first developed by Thurber [14]. It was based on the theoretical description developed by Freed and Heller [20] and studied by Wilson et al. and Yuen et al. [21, 22]. This model combined the effects of temperature, pressure, and excitation wavelength and was successfully used to predict the FQY of tracers like acetone and 3-pentanone. The processes of exciting and decay of a molecule are presented in Jablonski's energy diagram, as shown in Fig. 1, within the different mechanisms (fluorescence, vibrational relaxation, ISC, and IC). The molecule was excited by a laser from the ground singlet state S_0 to the excited singlet S_1. The excess vibrational energy E_1 of the molecule reached in the excited singlet state (S_1) is calculated from its initial thermal energy $E_{thermal}^0$ at ground state, the laser excitation energy $E_{laser,}$ and the energy gap between the excited and ground singlet states. Here, E_0 is equal to 36,386 cm^{-1} for anisole [23]:

$$E_1 = E_{thermal}^0 + E_{laser} + E_0. \tag{2}$$

In the ground or excited singlet state S_0/S_1, the molecule contains an average vibrational energy $E_{thermal}$ (cm^{-1}) calculated from its vibrational modes:

$$E_{thermal} = \sum_{i=1}^{n} \frac{\omega_i}{\exp\left(\frac{hc\omega_i}{kT}\right) - 1} \tag{3}$$

with ω_i the vibrational frequency of the molecule, h Planck constant, c the light velocity, and k Boltzmann constant. Anisole has 42 vibrational frequencies at ground/excited state and the detailed frequencies are listed in Table 1 [23].

The laser excitation energy E_{laser} depends on the excitation wavelength λ, and the 10^7 arises from the unit conversion from nanometer to centimeter:

$$E_{laser} = \frac{10^7}{\lambda}. \tag{4}$$

From the excited singlet vibrational energy level E_1, the excited molecule relaxes through a sequence of vibrational energy levels E_i, which is caused by relaxation collision and is determined by the energy transferred per collision, where a linear dependence of the excess energy above the thermal equilibrium is assumed:

Fig. 1 Simplified model of photophysical behavior, with a multistep decay of the excited single. The diagram presents the various collisional rates and processes [14]
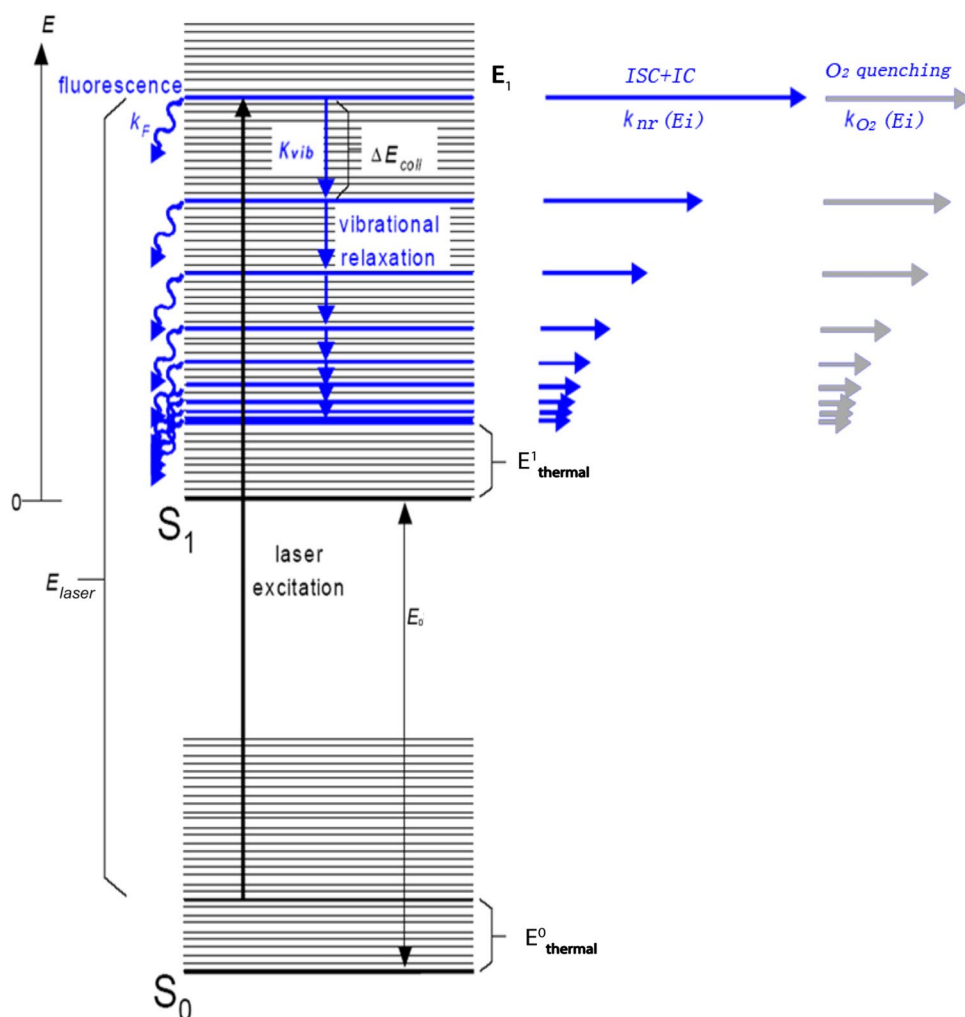
Table 1 Summary of calculated frequencies of the harmonic normal mode in S_0 and S_1 states [23]

Assignment	Frequency (cm^{-1})		Assignment	Frequency (cm^{-1})		Assignment	Frequency (cm^{-1})	
	S_1	S_0		S_1	S_0		S_1	S_0
T(methoxy internal rotation)	88	92	17a	671	946	19b	1415	1456
10b	162	203	5	841	965	CH$_3$antisym. def.	1463	1460
β (COC bending)	247	251	12	944	988	CH$_3$ scissoring	1474	1475
t (methyl internal rotation)	221	267	18a	961	1020	19a	1465	1498
16a	172	416	O–CH$_3$ stretching	1036	1045	8b	1234	1592
15	418	437	18b	998	1079	8a	1561	1612
16b	362	509	CH$_3$ twisting	1154	1146	CH$_3$ sym. stretching	2880	2934
6a	523	549	9b	1076	1153	CH$_3$ antisym. stretching	2944	2990
6b	499	616	9a	1133	1169	CH$_3$ antisym. stretching	2986	3063
4	529	689	CH$_3$ rocking	1179	1179	7a	3020	3094
11	634	750	13	1288	1249	7b	3036	3101
1	757	782	3	1629	1306	20a	3046	3117
10a	526	811	14	1333	1328	20b	3060	3125
17b	713	877	CH$_3$sym. def.	1424	1445	2	3071	3135

$$E_{i+1} = E_i - \Delta E_{i,coll}. \tag{5}$$

Equation (6) determines the distance between the level i in the vibrational energy cascade and the level $i + 1$:

$$\Delta E_{i,coll} = \alpha(E_i - E^1_{thermal}) \tag{6}$$

where α is the vibrational relaxation energy cascade coefficient which depends on the collision partner. A lower value of α indicates a decrease of the energy rate transferred by vibrational relaxation and increases the number of excited singlet levels used in the model. From every vibrational level, the following types of energy transferring processes are considered: the fluorescence defined by the fluorescence rate k_{fl}, the combined ISC and IC defined by the common non-radiative rate k_{nr}, the vibrational relaxation defined by the rate k_{vib}, and the collisional oxygen quenching characterized by the quenching rate k_{O2} that proportional to the oxygen number density. This calculation allows the most important physical processes to be calculated separately and the incorporated influence of temperature and pressure to be highlighted.

As expressed in Eq. (7), the FQY(Φ) is modelled at the sums of all over the N vibrational levels in the excited singlet occupied by the molecule as it decays, with the level 1 being the initially excited state and the level N a state sufficiently close to the thermalized level:

$$\Phi = \frac{k_{fl}}{k_{fl} + k_{vib} + k_{nr,1} + k_{0_2,1}}$$
$$+ \sum_{i=2}^{N-1} \left[\frac{k_{fl}}{k_{fl} + k_{vib} + k_{nr,i} + k_{0_2,i}} \prod_{j=1}^{i-1} \left(\frac{k_{vib}}{k_{fl} + k_{vib} + k_{nr,j} + k_{0_2,j}} \right) \right]$$
$$+ \frac{k_{fl}}{k_{fl} + k_{nr,N} + k_{0_2,N}} \prod_{j=1}^{N-1} \left(\frac{k_{vib}}{k_{fl} + k_{vib} + k_{nr,j} + k_{0_2,j}} \right). \tag{7}$$

The fluorescence rate k_{fl} from the excited singlet state may vary with the excitation energy due to changing Frank–Condon factors across the vibrational manifold. Therefore, it could be function of vibrational levels if sufficient fluorescence lifetime and non-radiative rate data are available. However, this rate is currently considered constant on any vibrational level, since weaker the symmetry of anisole, where the fluorescence rate of anisole is assumed to 2.89×10^7 s^{-1} [23].

The vibrational relaxation rate (k_{vib}) depends on the experimental conditions (colliders B and tracer A) and summation is performed on the colliders' number, which is given by

$$k_{vib} = \sum_i k_{vib}^{A/B_i} = \sum_i \left(\frac{X_{B_i} P}{kT} \right) Z_{coll_i} \tag{8}$$

where P is the total pressure, T is the temperature, X_{Bi} is the molar fraction of the collider i, k is Boltzmann constant, and Z_{coll} is the Lennard–Jones collision frequency for the collider i expressed by the following equation:

$$Z_{coll} = \pi \sigma_{AB}^2 \left[\frac{8RT}{\pi M_{AB}} \right]^{1/2} \Omega_{AB} \tag{9}$$

with the universal gas constant R, the Lennard–Jones collision diameter σ_{AB}, the reduced molar weight M_{AB}, and the collision integral Ω_{AB} between the tracer A and the collider B. In this paper, the collider is mainly O_2, N_2, CO_2, and Ar, as the four bath conditions investigated. σ_{AB} is the mean value of σ_A and σ_B, calculated from the critical temperature T_c and pressure P_c of anisole [23] with N Avogadro number:

$$\sigma = \left(\frac{3}{2} \cdot \frac{18.4 \frac{T_c}{P_c}}{\pi N} \right)^{1/3}. \tag{10}$$

The collision integral Ω_{AB} is calculated from Neufield relation [24]:

$$\Omega_{AB} = \frac{A}{(T*)^B} + \frac{C}{\exp{(DT*)}} + \frac{E}{\exp{(FT*)}} + \frac{G}{\exp{(HT*)}} \tag{11}$$

with $A = 1.06036$, $B = 0.15610$, $C = 0.19300$, $D = 0.47635$, $E = 1.03587$, $F = 1.52996$, $G = 1.76474$, $H = 3.89411$, and $T*$ is the reduced temperature:

$$T* = \frac{kT}{\varepsilon_{AB}} \tag{12}$$

where

$$\varepsilon_{AB} = (\varepsilon_A \varepsilon_B)^{1/2} \tag{13}$$

with ε_A and ε_B the potential well depths of tracer A and collider B [24], which are listed in Table 2.

The reduced molar weight M_{AB} is defined as follows:

$$M_{AB} = \frac{2}{1/M_A + 1/M_B}. \tag{14}$$

Table 2 List of potential well depths incorporated in this anisole model calculation

	Anisole	O_2	CO_2	N_2	Ar
$\varepsilon * 10^{21}$[J]	6.86	1.64	3.23	1.34	1.60

As for the vibrational relaxation rate, the collisional quenching rate k_{O2} is estimated from the Lennard–Jones collision frequency:

$$k_{o_2,i} = Z_{coll}\langle p \rangle n_{o_2} \tag{15}$$

where Z_{coll} is calculated by Eq. (9), n_{O2} is the oxygen number density, and $<p>$ represents the collision probability with oxygen and depends on energy level i of the excited molecule. Compared to the original model developed by Thurber [14] and Koch [13], the current work intends to optimize the following parameters in anisole model: the common non-radiative rate $k_{nr,i}$, the collision probability with oxygen $<p>$, the vibrational relaxation energy cascade coefficient α, and the equivalent IVR rate.

2.2 Anisole model development

2.2.1 Non-radiative rate

The non-radiative rate $k_{nr,i}$ decreases with increasing energy difference between the quantum states. The overlap of the vibrational wave functions decreases with increasing energy gap, which explains that the ISC of ketones is much faster than that of PAHs [4]. At low pressure, collisions occur at a rate that is too low to affect significantly the energy of the excited molecules before they decay due to non-radiative phenomena. In this case, the effective fluorescence time at specific energy level i is given by

$$\tau_{eff} = \frac{1}{k_{fl} + k_{nr,i}}. \tag{16}$$

Recently, Benzler et al. [19] provided a set of anisole effective fluorescence lifetimes with several temperatures (296, 355, 405, and 475 K) at pressure of 10 mbar in $CO_2/$

anisole mixtures via the fast pulse laser. Thus, based on these experimental results, provided with the constant fluorescence rate of $2.89 \times 10^7 \, s^{-1}$, the non-radiative rate variation with excess vibrational energy is inferred by Eq. (16), as shown by the blue stars in Fig. 2. Thus, Eq. (17) shows the optimized non-radiative rate $k_{nr,i}$ using an optimization algorithm to minimize the least squares, which is deduced from the experimental fluorescence lifetime measurements reported by Matsumoto et al. [23] and Benzler et al. [19] for an excess energy from 0 to 8000 cm^{-1}:

$$k_{nr,i} = 2.837 \times 10^7 * \exp(0.00032 E_i). \tag{17}$$

This evolution is similar to the exponential function widely used for acetone [14] or 3-pentanone [13].

2.2.2 Collision probability with oxygen

The collision probability $<p>$ used to calculate the collisional quenching rate k_{O2} [cf. Eq. (15)] is normally considered as the quenching efficiency or the probability that a collision will result in a quenching event. It is then reasonable to describe the collision probability as a function of the electronic energy. The expressions for the collision probability with oxygen $<p>$ for the current and previous studies are presented in Table 3. Koch [13] used a step increase model at 11,000 cm^{-1}.

2.2.3 Vibrational relaxation energy cascade coefficient

The vibrational relaxation energy cascade coefficient α allows to determine the distance between the level i in the vibrational energy cascade and the level $i + 1$ [cf. Eq. (6)]. For acetone fluorescence model, Thurber

Fig. 2 Evolution of the non-radiative rate for anisole versus the excess energy from data of Matsumoto et al. [23] and Benzler et al. [19]
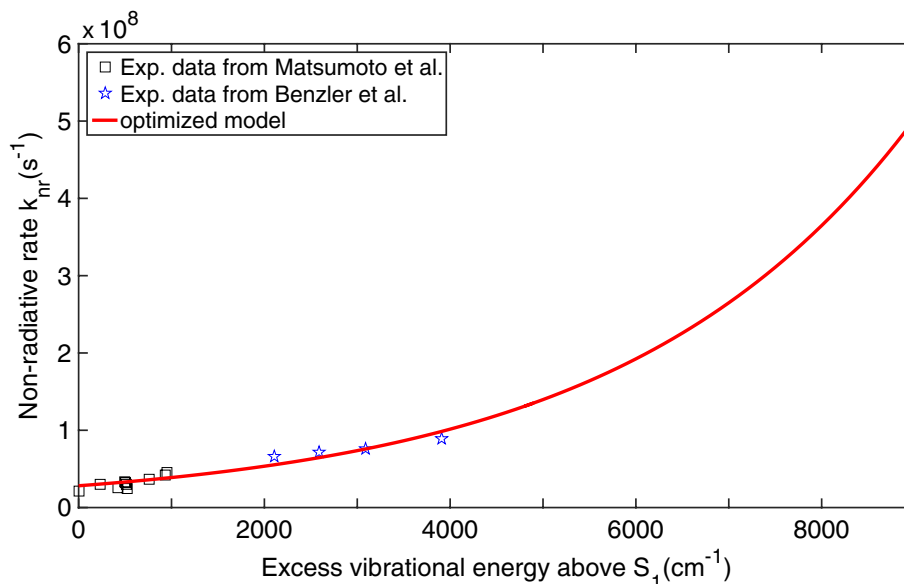
Table 3 Oxygen quenching probability, comparison with the expressions established by Koch [13], Cheung and Hanson [12]

Tracers	Oxygen quenching probability
Anisole (current)	$\langle p \rangle = 8 \times 10^{-2} \exp \left(E_i / 10^5 \right)$
3-pentanone [13]	$\langle p \rangle = 0.0023 \exp \left(5 \times 10^{-5} E_i \right), E_i \leq 11000 \ \text{cm}^{-1}$
	$\langle p \rangle = 0.25, E_i \geq 11000 \ \text{cm}^{-1}$
3-pentanone [12]	$\langle p \rangle = 0.00190 \exp \left(E_i / 20408 \right)$

[14] used constant values according to the bath gas: $\alpha = 0.032$ (in nitrogen) and $\alpha = 0.063$ (in air). However, Koch [13] developed the following temperature dependence for 3-pentanone:

$$\alpha = 0.05(T/300)^{-1.2}. \tag{18}$$

Furthermore, Cheung and Hanson [12] found an underestimation of absolute fluorescence with the pressure variation, where only temperature dependence is considered in α and thus optimized cascade coefficient with a temperature and vibrational energy dependence according to collisions with nitrogen and oxygen for 3-pentanone:

$$\alpha_{N_2} = \left[0.900 \exp \left(-\frac{T}{82.18} \right) + 0.0035 \right]$$
$$\times \left[0.0027 \exp \left(\frac{E_i}{2150} \right) + 0.95 \right] \tag{19}$$

$$\alpha_{o_2} = \left[3.341 \exp \left(-\frac{T}{59.22} \right) + 0.00503 \right]$$
$$\times \left[0.0027 \exp \left(\frac{E_i}{2150} \right) + 0.95 \right]. \tag{20}$$

Moreover, it is shown that the rate of energy loss changes with the vibrational energy when it approaches the thermal energy level in studies with toluene, azulene, and pyrazine [26–28].

In the present anisole model, the new α is obtained by adjusting the model to fit the experimental results. However, it safely assumed as a function of temperature and vibrational energy level:

$$\alpha = 0.5 \times \left(\frac{T}{1100} \right)^{-3} \times \left[0.009 \exp \left(\frac{E_i}{1600} \right) + 0.65 \right]. \tag{21}$$

Noted that both temperature and vibrational energy dependences are indifferent to the bath gases in our studies, which are consistent with the previous studies of Koch [13] and Cheung and Hanson [12].

2.2.4 Intramolecular vibrational redistribution (IVR) for anisole

Studies of anisole vibrational spectroscopy have shown that the aromatic ring substitution leads to an acceleration of Intramolecular Redistribution of Vibrational energy [23, 25]. This energy repartition (obtained at high-temperature and high-pressure excitation) in the molecule between aromatic ring and methoxy group is very fast:IVR time is included between 30 and 100 ps, while the fluorescence time is 19 ns [23]. In anisole molecule, there are two transition types $S_1 \rightarrow S_0$: radiative transition by the aromatic ring and the transition without radiation by the O–CH$_3$ group. During the molecule excitation, radiative transition of aromatic group obtains more energy than methoxy group. This promotes a faster redistribution of intramolecular energy in the anisole. Intramolecular collisions in asymmetric manner decrease the energy, leading to a new redistribution. As indicated by Smalley [29], this process is extremely fast which accelerates the internal conversion. Similar results have been found by Borst and Pratt [30], who have investigated $S_1 \rightarrow S_0$ electronic transitions of toluene and toluene-d$_3$. These authors indicated the energy interaction between the benzene ring and the methyl group in the state S_1 results in an IVR, which affects the subsequent fluorescence radiation in terms of final FQY. Since these experimental evidence and investigations, an equivalent Intramolecular Vibrational Redistribution rate deserves to be proposed, and it is in purpose of accounting the fluorescence loss caused by vibrational energy redistribution. Since it indeed dose not appears to compete with other de-excitation process in the time scale, we name it as the "equivalent" one. Moreover, it is estimated as a function of pressure, temperature, and excess energy level, and to achieve good compatibility with the present step-ladder modelling, this equivalent IVR is taken account by the way of competition with other de-excitation phenomena on every excess energy level.

Therefore, in our study, the applied FQY model calculates equation as follows:

$$\Phi = \frac{k_{\text{fl}}}{k_{\text{fl}} + k_{\text{vib}} + k_{0_2} + k_{nr,1} + k_{\text{IVR},1}}$$
$$+ \sum_{i=2}^{N-1} \left[\frac{k_{\text{fl}}}{k_{\text{fl}} + k_{\text{vib}} + k_{0_2} + k_{\text{nr},i} + k_{\text{IVR},i}} \prod_{j=1}^{i-1} \left(\frac{k_{\text{vib}}}{k_{\text{fl}} + k_{\text{vib}} + k_{0_2} + k_{\text{nr},j} + k_{\text{IVR},j}} \right) \right] \tag{22}$$
$$+ \frac{k_{\text{fl}}}{k_{\text{fl}} + k_{0_2} + k_{\text{nr},N} + k_{\text{IVR},N}} \prod_{j=1}^{N-1} \left(\frac{k_{\text{vib}}}{k_{\text{fl}} + k_{\text{vib}} + k_{0_2} + k_{\text{nr},j} + k_{\text{IVR},j}} \right).$$

Felker and Zewail [31] found the vibrational state density as an exponential function of the excess energy and defined three manifestations of IVR (absent, restricted, and dissipative) by different excess energy regimes within jet-cooled anthracene spectra studies. Similarly, in the present paper, the equivalent IVR rate is assumed as excess energy dependence could well inherit the IVR process characteristics. In addition, theoretically, the higher pressure promotes the stronger molecule collision intensity, which enhances the energy transfer between the benzene ring and methoxy group and results in the lower FQY. Besides that, the methyl group rotor decreases the onset energy level of vibrational state mixing [32], which is closely intimated with temperature condition of the gaseous molecular. Therefore, it is reasonable to further optimize the equivalent IVR rate through the introduction of pressure and temperature dependences:

$$k_{\text{IVR}}(T, P, E_i) = 3.6 \times 10^4 \times \exp\left(\frac{T}{65}\right) * \left[1 - \exp\left(-\frac{P}{10}\right)\right]$$
$$* \left[0.009 \exp\left(\frac{E_i}{1600}\right) + 0.65\right]. \tag{23}$$

Consequently, the equivalent IVR rate is formulated by Eq. (23). Noted that the excess energy dependence item is identical to that of vibrational relaxation energy cascade coefficient for the self-consistency consideration. Moreover, two exponential functions expressed the potential temperature and pressure impact on vibrational state mixing. Apparently, the equivalent IVR rate assumes a positive correlation to temperature and pressure. As a result, the optimized rates and parameters used in the anisole FQY model are summarized in Table 4.

3 Experimental measurements and uncertainties

Experimental fluorescence signal measurements were conducted in a high-pressure and high-temperature (HP–HT) cell with temperature and pressure ranges of 473–823 K and 0.2–4 MPa at the excitation wavelength of 266 nm. The experimental schematic and procedures are described in detail in [8] and are just briefly reminded here. During experiments, anisole is diluted in isooctane,

Table 4 Summary of different rates and parameters used in the anisole FQY model

Model parameter	Anisole
Energy cascade coefficient	$\alpha = 0.5 \times \left(\frac{T}{1100}\right)^{-3} \times \left[0.009 \exp\left(\frac{E_i}{1600}\right) + 0.65\right]$
Fluorescence rate (s^{-1})	$k_{\text{fl}} = 2.89 \times 10^7$
Non-radiative rate (s^{-1})	$k_{\text{nr},i} = 2.837 \times 10^7 * \exp(0.00032 E_i)$
Vibration relaxation rate (s^{-1})	$k_{\text{vib}} = \sum_i k_{\text{vib}}^{A/B_i} = \sum_i \left(\frac{X_{B_i} P}{kT}\right) Z_{\text{coll}_i}$ A: anisole; B: N_2, CO_2, Ar
Oxygen quenching probability	$\langle p \rangle = 8 \times 10^{-2} \exp\left(E_i / 10^5\right)$
Intramolecular vibrational redistribution rate (s^{-1})	$k_{\text{IVR}}(T, P, E_i) = 3.6 \times 10^4 \times \exp\left(\frac{T}{65}\right) * \left[1 - \exp\left(-\frac{P}{10}\right)\right] * \left[0.009 \exp\left(\frac{E_i}{1600}\right) + 0.65\right]$

Table 5 Experimental conditions for the anisole fluorescence measurement

Tracer	P (MPa)	T (K)	Molecular concentration (molecules/cm^3)	Bath gas	λ (nm)	E_{laser} (mJ/pulse) at 10 Hz
Anisole	0.2–4	473–823	2.58×10^{16}	N_2, Ar CO_2, O_2	266	90

and the liquid mixture of anisole (C_7H_8O)/isooctane (C_8H_{18}) is injected via a micrometric syringe of a 1 mL volume and a capillary tube into the chamber and then vaporized by reaching the tracer vapor pressure according to the temperature through a vacuum pump. The fluorescence signal is analysed by a high sensitivity spectrometer (motorized slit, three diffraction gratings of 150, 600, and 1200 grooves per mm, and the integration time of 150 μs). The experimental conditions (pressure, temperature, molecular concentration of the tracer, bath gas, excitation wavelength, and laser energy) explored for the anisole are summarized in Table 5.

Estimation of the measurement uncertainties was calculated from the uncertainty contribution of each term in the expression of the fluorescence signal S_f in manner of collected photons:

$$S_f = \frac{E}{hc/\lambda}\eta_{opt}dV_c\left[\frac{xP}{kT}\right]\sigma(\lambda, T)\Phi\left(\lambda, T, P, \sum_i x_i\right) \quad (24)$$

where E is the laser fluence (J m^{-2}), (hc/λ) is the energy of a photon (J) at the excitation wavelength λ (nm), η_{opt} is the overall efficiency of the collection optics, dV_c is the collection volume (cm^3), σ is the molecular absorption cross section of the tracer (cm^2), Φ is the fluorescence quantum yield, x is the mole fraction, P is the total pressure (Pa), k is the Boltzmann constant (J K^{-1}), and T is the temperature (K). Measurement uncertainties on the fluorescence signal are then given by

The absorption cross section, the mole fraction, and the pressure represent the most important contribution to the uncertainty. The measurement uncertainty for anisole [8] is

$$6.8\% \leq \frac{\Delta S_f}{S_f} \leq 8.5\%. \quad (26)$$

4 Comparison between the measured fluorescence signal and the calculated FQY from the current models for anisole

4.1 Pressure dependence of anisole FQY model

The pressure influence on anisole FQY model is underlined in Fig. 3. To compare with the model results, the experimental fluorescence signal normalized to the molecular density and the reference pressure at 0.2 MPa is noted S_f^* at fixed temperature and excitation wavelength, which is proportional to the experimental FQY. The scatter points indicate the experimental results at four temperatures with uncertainties. In addition, the phenomenological anisole model results (dash lines) proposed by Faust et al. [9] are presented in Fig. 3 as well.

Globally, both our model (solid lines) and Faust model (dash lines) well predict the anisole FQY decrease trend with increasing pressure. However, at high temperature, e.g., 773 K, both models show some deviations to the
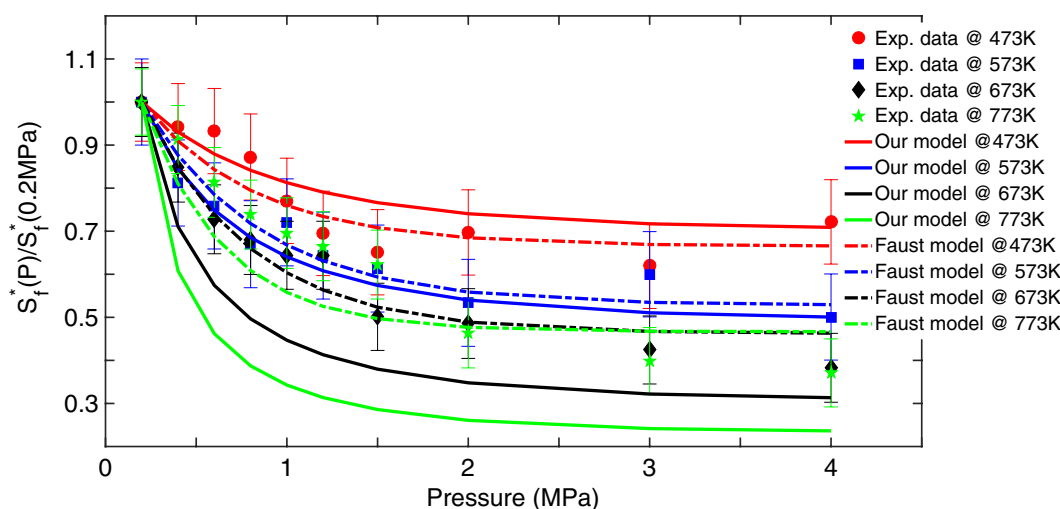
$$\frac{\Delta S_f}{S_f} = \sqrt{\left(\frac{\Delta E}{E}\right)^2 + \left(\frac{\Delta\lambda}{\lambda}\right)^2 + \left(\frac{\Delta\eta_{opt}}{\eta_{opt}}\right)^2 + \left(\frac{\Delta V_c}{V_c}\right)^2 + \left(\frac{\Delta x}{x}\right)^2 + \left(\frac{\Delta P}{P}\right)^2 + \left(\frac{\Delta T}{T}\right)^2 + \left(\frac{\Delta\sigma}{\sigma}\right)^2 + \left(\frac{\Delta\Phi}{\Phi}\right)^2}. \quad (25)$$

Fig. 3 Variations of experimental and model FQY with the pressure for anisole excited at 266 nm in nitrogen for different temperatures. For each temperature, the signal S_f^* is normalized to the molecular density and the reference value at 0.2 MPa (experimental data: *scatter points*; our model: *solid lines*; and Faust model: *dash lines*)
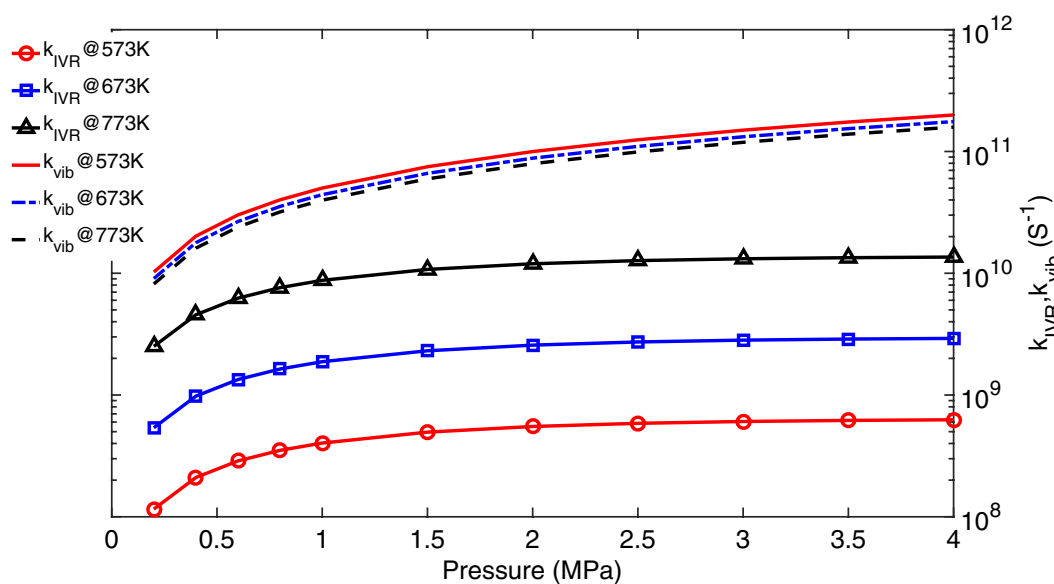
Fig. 4 Evolutions of k_{IVR} and k_{vib} with the pressure for different temperatures in nitrogen (the k_{IVR} is calculated on the energy level of 8630.2 cm^{-1})

Fig. 5 Variations of experimental and model FQY with the temperature for anisole excited at 266 nm in nitrogen for different pressures. For each pressure, the signal S_f^{**} is normalized to the molecular density, the absorption cross section, and the reference value at 473 K. (experimental data: *scatter points*; our model: *solid lines*; Faust model: *dash lines*)
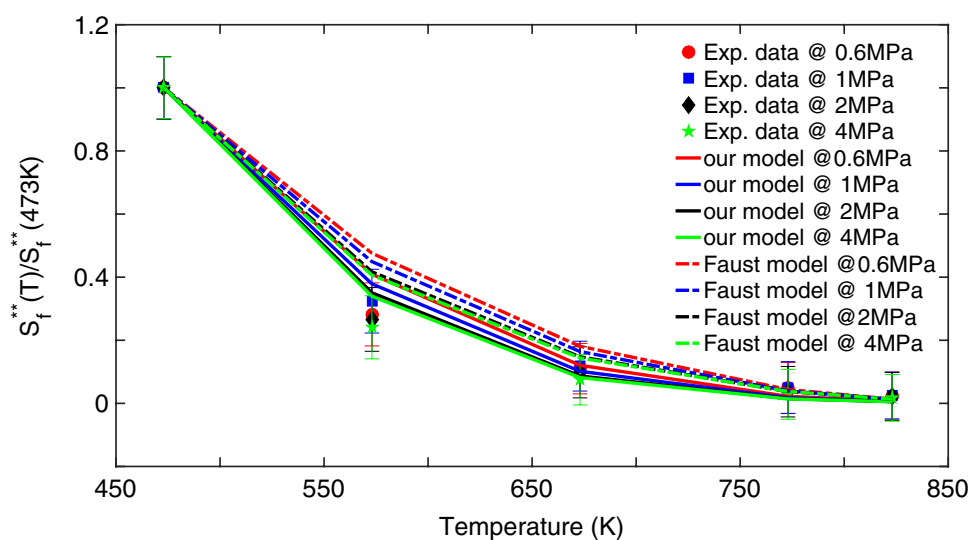
experimental data. This is not only attributed to experimental random errors, also the model precision. The underestimation of FQY in our model at high temperature is probably due to the overestimated of non-radiative rate.

Moreover, the fluorescence signal decreases faster when the pressure is below 2 MPa than that above 2 MPa, which is observed in both the experimental and model results. This evolution is mainly attributed to the competition of IVR process with other depopulation processes. The detailed interpretation is as follows: when the pressure is above 2 MPa, the acceleration of vibrational relaxation process weakens the signal decrease, while IVR and the non-radiative process are not favored, then a slight FQY

reduction is achieved. This could be corroborated by the evolution of k_{IVR} and k_{vib} with the pressure in nitrogen, as shown in Fig. 4. With the pressure increase from 0.2 to 4 MPa, k_{vib} increases faster than k_{IVR}, and the gap between both energy relaxation rates increases for any temperature considered. Fortunately, this high-pressure influence is very good predicted by the current anisole model.

4.2 Temperature dependence of anisole FQY model

Figure 5 presents the temperature dependence of the model calculated FQY and the experimental fluorescence signal for anisole at different pressures in nitrogen. The

Fig. 6 Evolution of k_{IVR} with temperature for different pressures (k_{IVR} is calculated on the energy level of 8630.2 cm^{-1}.)
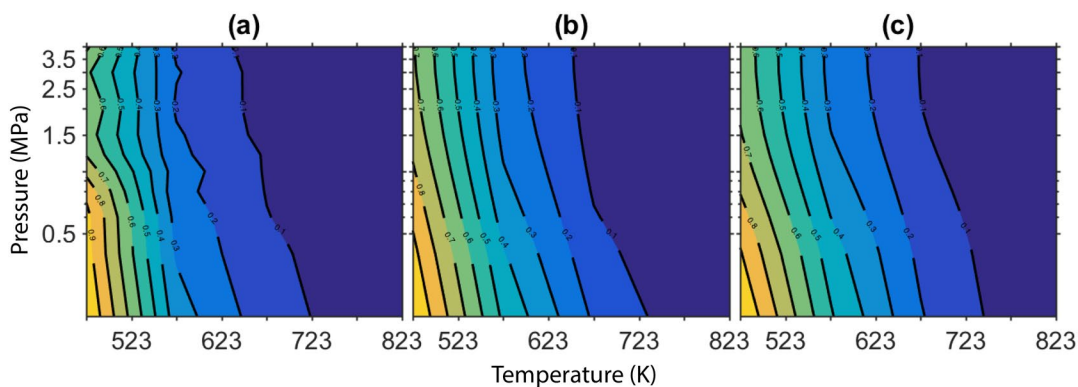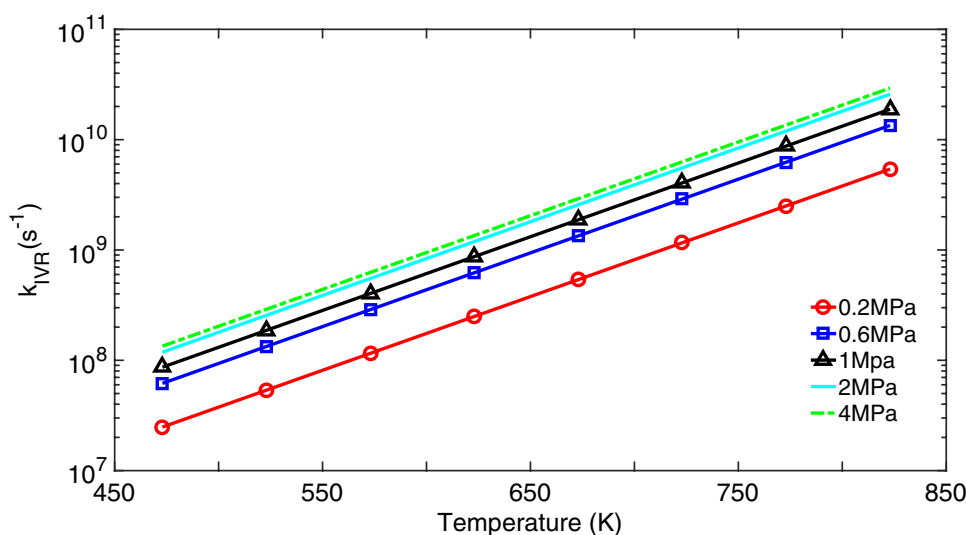

Fig. 7 Map of normalizedexperimental (a), our model (b), and Faust model(c) FQY for anisole in nitrogen. All FQYs are normalized to the respective reference value at 473 K and 0.2 MPa

experimental data are normalized to the molecular density, the absorption cross section, and the reference value at 473 K and is noted S_f^{**}. It represents the experimental FQY. Within the temperature rising, the non-radiated depopulation processes strengthen and the FQY drops. Our model and Faust model well predict the experimental results within the temperature range even with these estimated errors. However, in Faust model, some overestimations at low temperature are observed. Figure 6 displays the temperature variation of anisole equivalent IVR rate for different pressures in nitrogen.

In addition, the experimental FQY decreases exponentially by two orders of magnitude for the studied temperature (473–823 K) and pressure range (0.2–4 MPa). Similar results were achieved with toluene [5] and fluoranthene [6] as tracers used in the temperature measurement. For anisole, the reason of the FQY sharp

dropping is either the more efficient non-radiative mechanism or the influence of the IVR.

Figure 7 represents the comparison of the normalized model FQY results with that of experimental one within the studied temperature and pressure range. Both models predict correctly the coupled influence of pressure and temperature on the FQY. The evolution of the fluorescence signal depends mainly on the temperature. The pressure influence on the FQY reduction is well transcribed by the model.

4.3 Bath gases dependence of anisole FQY model

The influence of the bath gases (N$_2$, CO$_2$ and Ar) on the FQY at 573 K is presented in Fig. 8. The current model (lines) describes the same trend as the experimental results (scatter points). Among all the experimental

Fig. 8 Comparison of experimental and our model FQY according to the pressure for anisole excited at 266 nm for different bath gases (N_2, CO_2, and Ar) at 573 K. For each bath gas, the signal S_f^* is normalized to the molecular density and the reference value at 0.2 MPa
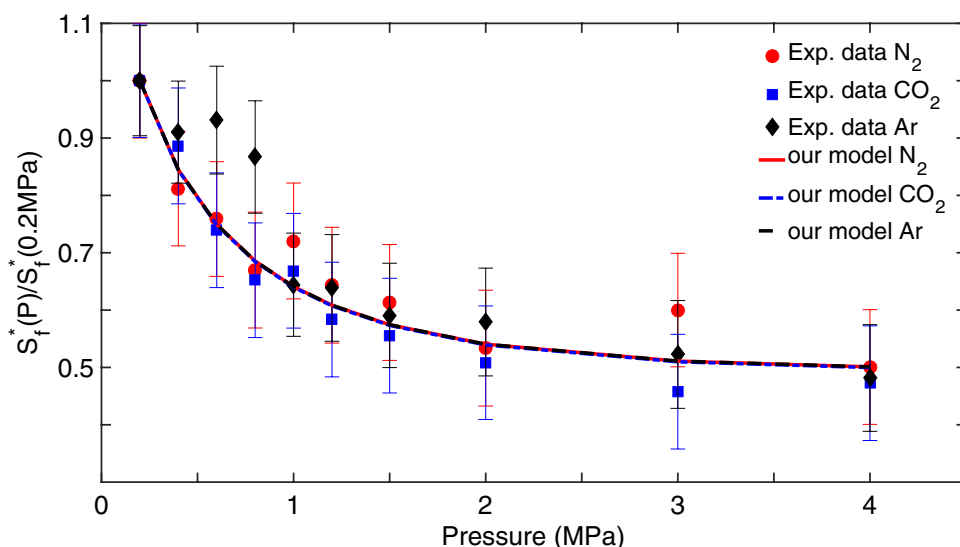
Fig. 9 Comparison of experimental and our model FQY according to the pressure for anisole at 523 K for three oxygen concentrations in nitrogen (10, 15, and 20%). For each condition, the experimental signal S_f^* is normalized to the reference value at 1 MPa
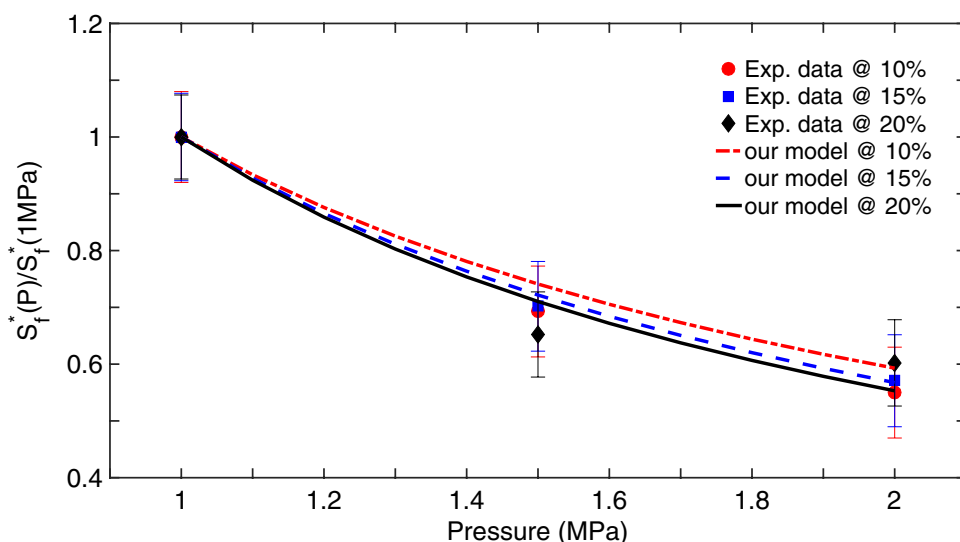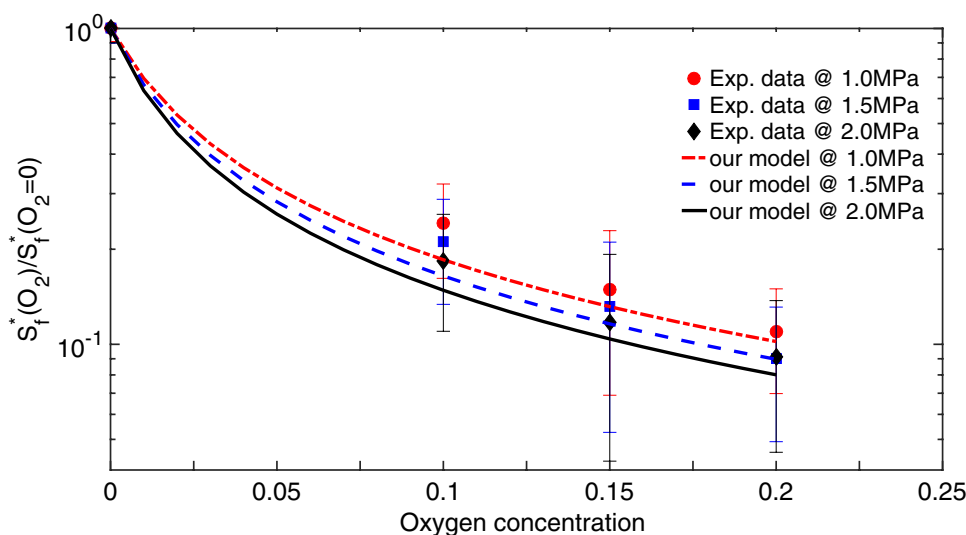
Fig. 10 Comparison of experimental and our model FQY according to the oxygen concentration in nitrogen for anisole at 523 K for three pressures (1.0, 1.5, and 2.0 MPa). For each pressure, the experimental signal S_f^* is normalized to the reference value at O_2 concentration of 0%

parameters, the pressure dependence of the FQY represents the most important contribution to the uncertainty ($5\% < \Delta P/P < 10\%$), which explains the important error bars in Fig. 8. With the increase of the bath-gas molar weight, the energy transportation during the collision is more important, which is successfully simulated by the calculation of vibrational relaxation rate. The discrepancy of the model results with experimental data according to the different colliders is only due to the k_{vib} calculation.

4.4 Oxygen quenching effects

The aromatics and PAHs like toluene and fluoranthene present strong de-excitation dependence with the oxygen concentration, mainly due to the longer fluorescence lifetime and the larger singlet–triplet energy gap in aromatics [3]. The Stern–Volmer constant evolutions of anisole have been evaluated in our previous studies [8].The strong dumping influence of temperature on Stern–Volmer constant implies the suitability of anisole for the measurement of local oxygen concentration and equivalence ratio. Figures 9 and 10 show the variations of the calculated anisole FQY results (lines) and experimental data (scatter points) versus pressure and oxygen concentration, respectively. In Fig. 9, for each oxygen concentration, the model well predicts the experimental fluorescence signal decreases with rising pressure. On the other hand, for a given pressure, both calculated FQY and experimental data decrease with higher oxygen concentration, as shown in Fig. 10. The anisole FQY model that combining the oxygen quenching rate well represents the experimental oxygen quenching trend. Noted that within oxygen concentration of 10–20%, the experimental data are less sensitive to the oxygen percentages, which may imply that the excited molecular depopulation by oxygen comes to a saturation status. In other words, the number of the formation of intermediate exciplex may be to a maximum level.

5 Conclusions

This study presents a fluorescence quantum yield model for anisole, which depends on thermodynamic parameters such as pressure, temperature, and bath gases. The current model takes into account the different phenomena such as the de-excitation by fluorescence, the common non-radiative rate, the vibrational relaxation, and the oxygen quenching, according to the energy level reached. The same anisole photophysical results (effective fluorescence lifetimes) in the literature are used to optimize the target de-excitation rate in the model, e.g., the common non-radiative rate. Moreover, the vibrational relaxation energy

cascade coefficient is modified by introducing vibrational energy dependence in addition to temperature dependence. An equivalent IVR rate is originally introduced in the FQY model for anisole, via considering the pressure, temperature, and vibrational energy level influence on the energy transition between the aromatic group and the methoxy group. It assumes a positive correlation to temperature, pressure, and vibrational energy level. Eventually, experimental data obtained in a high-pressure and high-temperature cell (0.1–4 MPa and 473–873 K) for different bath gases (N_2, CO_2, Ar and O_2) in previous studies are used to validate this proposed model.

As a result, the pressure increases the vibrational relaxation rate and the equivalent IVR rate, the opposing effects of these processes resulting in the slight decay of the FQY above 2 MPa, which is corroborated by the experimental results. Moreover, the model well predicts the temperature influence on the anisole fluorescence signal reduction. In the different bath gases (N_2, CO_2, and Ar), the current model describes the same trends as experimental results for anisole and the influence of the ambient gas on the FQY is successfully modelled by the calculation of the different k_{vib} rates. Finally, the oxygen quenching effect on the anisole fluorescence lies in the longer fluorescence lifetime and larger singlet–triplet energy gap, which is more attractive for the measurement of local oxygen concentration and equivalence ratio. The good agreement between the anisole model combined with oxygen quenching and experimental results further evaluates the validity of the current model.

References

1. S. Einecke, C. Schulz, V. Sick, Measurement of temperature, fuel concentration and equivalence ratio fields using tracer LIF in IC engine combustion. Appl. Phys. B **71**, 717–723 (2000)
2. M. Luong, R. Zhang, C. Schulz, V. Sick, Toluene laser-induced fluorescence for in-cylinder temperature imaging in internal combustion engines. Appl. Phys. B **91**, 669–675 (2008)
3. J. Reboux, D. Puechberty, F. Dionnet, A new approach of PLIF applied to fuel/air ratio measurement in the compression stroke of an optical S.I engine. SAE technical paper series, n° 941988 (1994)
4. C. Schulz, V. Sick, Tracer-LIF diagnostics: quantitative measurement of fuel concentration, temperature and fuel/air ratio in practical combustion systems. Prog. Energy Combust. Sci. **31**, 75–121 (2005)
5. W. Koban, J. Koch, R.K. Hanson, C. Schulz, Absorption and fluorescence of toluene vapor at elevated temperatures. Phys. Chem. Chem. Phys. **6**, 2940–2945 (2004)

6. M. Kühni, C. Morin, P. Guibert, Predicting fluorescence signal for fluoranthene in engine conditions: comparison of experimental and model results, in European Combustion Meeting ECM 2011, Cardiff, Wales, June 28–July 1 (2011)

7. A. V. Menon, Effect of m-xylene on soot formation in high pressure diffusion flames. Ph.D. thesis Pennsylvania State University (2010)

8. K.H. Tran, C. Morin, M. Kühni, P. Guibert, Fluorescence spectroscopy of anisole at elevated temperatures and pressures. Appl. Phys. B **115**, 461–470 (2014)

9. S. Faust, T. Dreier, C. Schulz, Photo-physical properties of anisole: temperature, pressure, and bath gas composition dependence of fluorescence spectra and lifetimes. Appl. Phys. B **112**, 203–213 (2013)

10. K.H. Tran, P. Guibert, C. Morin, J. Bonnety, S. Pounkin, G. Legros, Temperature measurements in a rapid compression machine using anisole planar laser-induced fluorescence. Comb. Flame **162**, 3960–3970 (2015)

11. V. Modica, C. Morin, P. Guibert, 3-pentanone LIF at elevated temperatures and pressures: measurements and modeling. Appl. Phys. B **87**, 193–204 (2007)

12. B.H. Cheung, R.K. Hanson, 3-pentanone fluorescence yield measurements and modeling at elevated temperatures and pressures. Appl. Phys. B **106**, 755–768 (2012)

13. J. Koch, Fuel tracer photophysics for quantitative planar laser-induced fluorescence. Ph.D. thesis Stanford University (2005)

14. M. Thurber, Acetone laser-induced fluorescence for temperature and multiparameter imaging in gaseous flows. Ph.D. thesis Stanford University (1999)

15. B. Rossow, Photophysical processes of organic fluorescent molecules and kerosene applications to combustion engines. Ph.D. thesis Université Paris-Sud 11 (2011)

16. R.R. Valiev, V.N. Cherepanov, V.Ya. Artyukhov, D. Sundholmb, Computational studies of photophysical properties of porphin, tetraphenylporphyrin and tetrabenzoporphyrin. Phys. Chem. Chem. Phys. **14**, 11508–11517 (2012)

17. V. Barone, J. Bloino, S. Monti, A. Pedone, G. Prampolini, Fluorescence spectra of organic dyes in solution: a time dependent multilevel approach. Phys. Chem. Chem. Phys. **13**, 2160–2166 (2011)

18. L.A. Barkova, V.V. Gruzinskii, M.N. Kaputerko, Quenching and stabilization of the fluorescence of anthracene vapor by xenon. J. Appl. Spectrosc. **47**, 786–789 (1987)

19. T. Benzler, S. Faust, T. Dreier, C. Schulz, Low-pressure effective fluorescence lifetimes and photo-physical rate constants of one- and two-ring aromatics. Appl. Phys. B **121**, 549–558 (2015)

20. K.F. Freed, D.F. Heller, Pressure dependence of electronic relaxation: a stochastic model. J. Chem. Phys. **61**, 3942–3953 (1974)

21. D.J. Wilson, B. Noble, B. Lee, Pressure dependence of fluorescence spectra. J. Chem. Phys. **34**, 1392–1396 (1961)

22. L.S. Yuen, J.E. Peters, R.P. Lucht, Pressure dependence of laser-induced fluorescence from acetone. Appl. Opt. **36**, 3271–3277 (1997)

23. R. Matsumoto, K. Sakeda, Y. Matsushita, T. Suzuki, T. Ichimura, Spectroscopy and relaxation dynamics of photoexcited anisole and anisole-d3 molecules in a supersonic jet. J. Mol. Struct. **735**, 153–167 (2005)

24. J.O. Hirschfelder, C.F. Curtiss, R.B. Bird, *Molecular Theory of Gases and Liquids* (Wiley, New York, 1954)

25. C.G. Eisenhardt, A.S. Gemechu, Excited state photoelectron spectroscopy of anisole. Phys. Chem. Chem. Phys. **3**, 5358–5368 (2001)

26. H. Hippler, J. Troe, H.J. Wendelken, Collisional deactivation of vibrationally highly excited polyatomic molecules. II. Direct observations for excited toluene. J. Chem. Phys. **78**, 6709–6717 (1983)

27. H. Hippler, B. Otto, J. Troe, Collisional energy transfer of vibrationally highly excited molecules. VI. Energy dependence of $< \Delta E >$ in azulene. Ber. Bunsenges. Phys. Chem. **93**, 428–434 (1989)

28. L.A. Miller, J.R. Barker, Collisional deactivation of highly vibrationally excited pyrazine. J. Chem. Phys. **105**, 1383–1391 (1996)

29. R.E. Smalley, Dynamics of electronically excited states. Ann. Rev. Phys. Chem. **34**, 129–153 (1983)

30. D.R. Borst, D.W. Pratt, Toluene: structure, dynamics, and barrier to methyl group rotation in its electronically excited state. A route to IVR. J. Chem. Phys. **113**, 3658–3669 (2000)

31. P.M. Felker, A.H. Zewail, Dynamic of intramolecular vibrational-energy redistribution (IVR). II. Excess energy dependence. J. Chem. Phys. **82**, 2961–2974 (1985)

32. C.G. Hickman, J.R. Gascooke, W.D. Lawrance, The S_1–S_0 ($^1B_2$–$^1A_1$) transition of jet-cooled toluene: excitation and dispersed fluorescence spectra, fluorescence lifetimes, and intramolecular vibrational energy redistribution. J. Chem. Phys. **104**, 4887–4901 (1996)